Journal of Colloid and Interface Science 487 (2017) 360–369

Contents lists available at ScienceDirect

Journal of Colloid and Interface Science

journal homepage: www.elsevier.com/locate/jcis

Regular Article

Reusable macroporous photonic crystal-based ethanol vapor detectors by doctor blade coating

Ya-Ling Ko [a], Hui-Ping Tsai [b], Kun-Yi Lin [c], Ying-Chu Chen [a], Hongta Yang [a,*]

[a] Department of Chemical Engineering, National Chung Hsing University, 145 Xingda Road, Taichung City 40227, Taiwan
[b] Department of Civil Engineering, National Chung Hsing University, 145 Xingda Road, Taichung City 40227, Taiwan
[c] Department of Environmental Engineering, National Chung Hsing University, 145 Xingda Road, Taichung City 40227, Taiwan

GRAPHICAL ABSTRACT

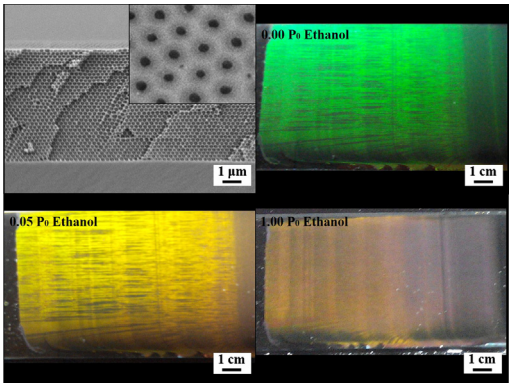

ARTICLE INFO

Article history:
Received 6 September 2016
Revised 17 October 2016
Accepted 22 October 2016
Available online 24 October 2016

Keywords:
Reusable
Photonic crystals
Self-assembly
Bragg diffraction
Vapor detection

ABSTRACT

This research reports the development of sensitive and reversible vapor detection by using three-dimensional macroporous photonic crystals. A scalable and roll-to-roll compatible doctor blade coating technology is utilized to fabricate flexible macroporous poly(ethoxylated trimethylolpropane triacrylate) (PETPTA) films with hexagonal close-packed pores which are interconnected. The pores are then coated with a layer of poly(2-hydroxyethyl methacrylate) (PHEMA) to create macroporous PHEMA/PETPTA films. The condensation of vapors in the PHEMA coated macroporous films leads to the increase of both the PHEMA swelling degree and the effective refractive index of the diffractive medium, resulting in the red-shift and amplitude reduction of the optical stop bands. The optical measurements reveal that the diffraction from the as-prepared macroporous photonic crystals sensitively monitors the vapor pressure of ethanol since the PHEMA layer displays a great volume dependence on ethanol due to a decreased Flory-Huggins mixing parameter. The dependence of the diffraction wavelength on vapor pressure and the reproducibility of vapor sensing have also been investigated in this study.

1. Introduction

To address rapidly-growing environmental issues and reduce increasingly serious chemosensory irritations in humans, detection and monitoring of volatile chemicals is critical for environmental

* Corresponding author.
E-mail address: hyang@dragon.nchu.edu.tw (H. Yang).

http://dx.doi.org/10.1016/j.jcis.2016.10.061
0021-9797/

monitoring, industrial emission control, chemical leak detection, and process monitoring applications [1–3]. Among various volatile chemicals, ethanol is one of the most concerning solvents, which is extensively used in the manufacturing industry, and commonly used as a biofuel additive for gasoline [4]. The ethanol vapor can lead to significant air pollution, involving substantial risks to biodiversity and adverse effects on human neurobehavioral functions [5,6]. Therefore, there is an urgent demand on ethanol vapor sensor developments.

In recent years, various semiconductors, conducting polymers, and electricity-based sensors have been extensively exploited for detecting ethanol vapor [7–9]. Nevertheless, the sensing methodologies suffer from complicated detection processes, high operating temperature, sensitivity to environmental factors, slow responses, and expensive detection equipments, which seriously restrict their developments [10–12]. In contrast, optical chemical sensing displays several advantages over other sensing methods, such as immunity to electromagnetic interface, low toxicity, non-invasiveness, and relatively inexpensive [13–15]. Owing to the novel structural colors and unique optical properties, photonic crystals, periodic dielectric structures with a forbidden gap for electromagnetic waves, have been explored for use in chemical vapor detections [16–18]. Capillary condensation of a condensable vapor in the voids of photonic crystals results in an increase of the effective refractive index of the diffractive medium, leading to a red-shift of the optical stop bands [19]. The reflection wavelength shift exhibits a linear relationship with vapor partial pressure, indicating that the colorimetric method offers a promising platform for chemical vapor sensing [20].

To date, a number of photonic crystal-based ethanol vapor sensors have been developed and exhibit great advantages in miniaturization, portability, short response time, on-line monitoring capability, security and stability [21–23]. However, the developments of photonic crystal-based sensors are impeded by the inferior vapor adsorption abilities and thus the sensitivity of vapor sensing are restricted [24,25]. To solve the problems, distinct surface groups, reagent dyes, or chemical indicators are employed to offer photonic crystals different responding properties, which providing higher sensitivity and selectivity towards the ethanol vapor [26–28]. Nevertheless, most of the preparations are relative complex and the displacement assays are time consuming. Moreover, once the labeled analyte is exhausted, refilling is needed unless the sensor will only be used once or for a short period of time. Recently, three dimensional periodically structured hydrogels, which are responsive to various chemical stimuli, have also been widely used as optical chemical sensors. The hydrogel swells in the presence of certain analytes, increasing lattice spacing, and consequently the diffraction peak shift towards longer wavelength. A number of strategies have been investigated to fabricate three dimensional ethanol-responsive hydrogel photonic crystals [29–33]. Although the vapor sensing performances are improved, the application and removal of stimuli leads to complex deformation of hydrogels, causing inhomogeneous expansion/shrinking with different magnitudes in different directions [34]. The deformation of samples results in deteriorated optical sensitivities of hydrogel photonic crystals. Furthermore, compared to complex lithography-based fabrication technologies, the use of spontaneous crystallization of monodisperse colloidal particles as templates is a simple and inexpensive approach for developing photonic crystals [35–37]. Unfortunately, most of the existing colloidal self-assembly methodologies, including capillary force-induced self-assembly, evaporation-induced convective assembly, assembly at the air-liquid interface, gravity sedimentation, and electrical field-induced self-assembly, suffer from low throughput and are favorable only for low volume, laboratory-scale production [38–44].

In this study, we report a sensitive and reversible detection of ethanol vapor by using three dimensional macroporous polymer photonic crystals, which are fabricated by a scalable and roll-to-roll compatible colloidal self-assembly approach. Most importantly, the as-prepared ethanol sensors featuring a highly visible readout are portable, small, handy, and readily responsive.

2. Scalable fabrication of macroporous photonic crystals

Three-dimensional (3D) macroporous polymer photonic crystals are fabricated by a scalable doctor blade coating technology [45]. Typically, monodispersed silica colloids are first synthesized by the StÖber method and then dispersed in ethoxylated trimethylolpropane triacrylate (ETPTA) monomer with 2-hydroxy-2-methyl-1-phenyl-1-propanone as a photo-initiator [46]. The silica colloid volume fraction is controlled to be 74 vol.%. A doctor blade is introduced to spread the silica colloidal suspension uniformly on a glass substrate, and to offer a one-dimensional shear force to align silica colloids [47]. The suspension is then photo-polymerized to obtain a silica colloidal crystal-polymer composite. As shown in Fig. 1, the embedded silica colloids can be etched away with a 1 vol.% hydrofluoric acid aqueous solution. The resulting macroporous polymer film is immersed in a mixture of 2-hydroxyethyl methacrylate (HEMA), methacrylic acid (MMA), polyethylene glycol (PEG), ethanol, and azobisisobutyronitrile (AIBN) as a photo-initiator, following by a spin-coating process to remove the HEMA mixture retained on the film surface. After storing in dark for one hour to allow residual ethanol to evaporate,

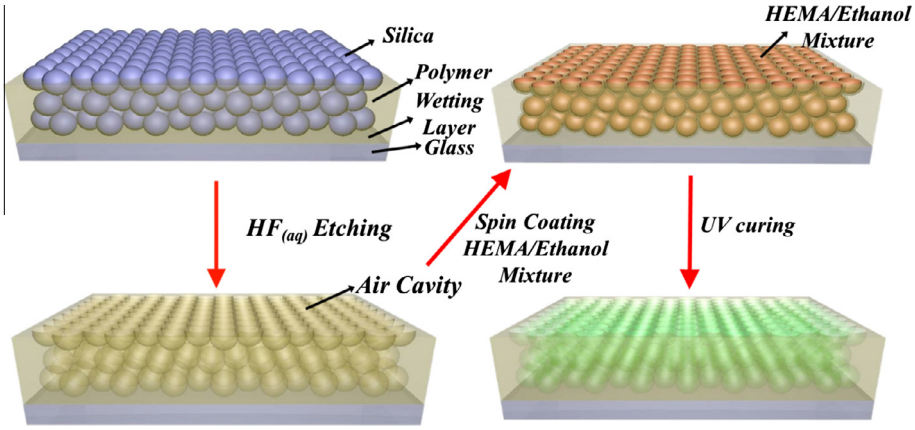

Fig. 1. The experimental procedure for fabrication of macroporous polymer photonic crystals.

the HEMA mixture is photo-polymerized to form a macroporous crosslinked poly(2-hydroxyethyl methacrylate)/poly(ethoxylated trimethylolpropane triacrylate) (PHEMA/PETPTA) film.

Fig. S1a displays a photograph of a doctor blade coated silica colloidal crystal-PETPTA composite consisting of 255 nm silica particles on a glass substrate illuminated with white light. The composite exhibits a striking yellow color caused by Bragg diffraction of incident visible light from the crystalline lattice. Although some defects appear, the long-range hexagonal ordering of silica colloidal crystals embedded in PETPTA matrix is evident from the scanning electron microscope (SEM) image as shown in Fig. S1b. The silica colloidal crystals of the shear-aligned composite can be selectively removed by hydrofluoric acid etching to create a macroporous PETPTA film. The macroporous film displays homogeneous shining blue color (Fig. S1c) caused by Bragg diffraction of blue light from the 3D highly ordered hexagonal close-packed air cavities in the film as displayed in Fig. S1d.

In order to further evaluate the optical properties of the doctor blade coated polymeric composite and the macroporous polymer film, an Ocean Optics UV–vis-NIR spectrometer (Dunedin, RH4000) is applied to measure the optical reflection at normal incidence. As shown in Fig. S2, compared with reflection spectrum of a featureless polymer film, the reflection spectra displays distinct peaks owing to Bragg diffraction from the 3D periodic structures. The positions of the diffraction peak can be theoretically estimated by using the Bragg's law [48]:

$$\lambda_{peak} = 2n_{eff} d \sin\theta$$

where n_{eff} is the effective refractive index of the medium, d is the inter layer spacing, and $\sin\theta$ equals to 1 at normal incidence. The calculated peak positions as indicated by the arrows agree well with the experimental results, confirming the highly crystalline quality of the self-assembled composite and the corresponding macroporous films. The diffraction efficiency of the composite is much lower than that of macroporous film because of the smaller refractive index between the silica particles ($n_{\text{silica}} = 1.42$) and polymer ($n_{\text{PETPTA}} = 1.46$).

3. Vapor-sensing macroporous PETPTA photonic crystals

The macroporous PETPTA film templated from 255 nm silica particles is placed in a sealed chamber, which is evacuated and then backfilled with a considerable volume of ethanol at a specific vapor pressure. Dry nitrogen is employed to maintain the total pressure in the chamber to be 1 atm. The normal-incidence specular reflectance spectra are obtained from the macroporous film exposed to vapors after 1 min. The time required for the achievement of vapor-liquid equilibrium inside the chamber is much lower than that in the experimental conditions [49]. Therefore, the changes of vapor phase composition in the system are negligible.

Fig. S3a shows that the diffraction of a macroporous PETPTA film with 255 nm air cavities red-shifts as the ethanol vapor pressure increases from 0 P_0 to 1 P_0 at 25 ± 1 °C, where P_0 is the saturation vapor pressure of ethanol at this temperature (60 mmHg) [50]. It is also found that the diffraction efficiency of that monotonically decreases with the increase in ethanol vapor pressure. The observed shift in color from blue to cyan and the amplitude reduction of the Bragg diffraction peaks result from more ethanol vapor condenses in the air cavities of the macroporous photonic crystals as the vapor pressure increases, leading to a higher effective refractive index of the diffractive medium and a lower dielectric contrast between the polymer and the enclosed materials. The vapor sensing can be extended to a wide variety of vapors, such as water. Fig. S3b reveals that the optical response of water vapor sensing is quite similar to that of ethanol vapor sensing. Compared to the macroporous film exposed to pure nitrogen, the shift of the diffraction peaks increases most linearly with vapor partial pressure (Fig. S3c). The linear correlation is critical to determine the vapor contents. Importantly, the optical properties of the macroporous photonic crystals can be fully recovered as the condensed liquid is evaporated and can thus be reused for vapor sensing.

To further determine the vapor condensation in the macroporous photonic crystals, the amounts of condensed liquid at different vapor partial pressures are estimated using the Bragg diffraction equation ($\lambda_{peak} = 2n_{eff} d \sin\theta$). The effective refractive index of the medium can be expressed as $n_{eff} = VF_{PETPTA} \times n_{PETPTA} + VF_{air} \times n_{air} + VF_{liquid} \times n_{liquid}$, where n_{PETPTA}, n_{air}, and n_{liquid} are refractive index of PETPTA (1.46), air (1.0), and condensed liquid, respectively. The volume fraction (VF) of PETPTA (VF_{PETPTA}) in the templated macroporous film consisting of closed-packed air cavities is 0.26, as a result that $VF_{air} = 0.74 - VF_{liquid}$. The volume fraction of condensed liquid (VF_{liquid}) at different vapor partial pressures can thus be estimated. Assuming the condensed liquid forms a uniform thin layer on the walls of the PETPTA voids, the thickness of the liquid layer is calculated using the estimated VF_{liquid}. As shown in Fig. S3d, the liquid layer thickness increases with vapor partial pressure. It is found that an about 23 nm condensed ethanol layer can be formed on the walls of 255 nm voids when the macroporous film is exposed to a saturated ethanol vapor (P/Po = 1), while a ~18 nm condensed water layer can be formed when the macroporous film is exposed to a saturated water vapor. The capillary condensation of vapor in the macroporous film can be qualitatively described by the Kelvin equation

$$\ln\frac{P}{P_o} = \frac{2V_m\gamma}{rRT}$$

where V_m is the molar volume of liquid, γ is the liquid/vapor surface tension, r is the radius of curvature, which equals to the radius of the air cavity minus the thickness of the liquid layer in macroporous films [51]. Consequently, a higher vapor partial pressure results in a smaller r and the formation of thicker liquid layer [52]. Additionally, the r is proportional to γ at a fixed P/P_0. This explains that the condensed ethanol liquid layer (γ_{ethanol} = 21.6 mN/m) is thicker than the condensed water liquid layer (γ_{water} = 72.9 mN/m) at same vapor partial pressure. However, the response of water vapor sensing is quite similar to that of ethanol vapor sensing. This issue greatly impedes the selectivity of vapor sensing in practical application and therefore should be further addressed.

4. Vapor-sensing of macroporous PHEMA/PETPTA photonic crystals

To trackle the challenge, the macroporous PETPTA film templated from 255 nm silica spheres is immersed in a 20 vol.% HEMA/ethanol mixture, following by a photo-polymerization procedure. The pores of macroporous PETPTA films are thus coated with a uniform layer of PHEMA, which is highly responsive to ethanol, to create macroporous PHEMA/PETPTA photonic crystals. As shown in Fig. 2a, the macroporous PHEMA/PETPTA film exhibits homogeneous shining green color resulted from Bragg diffraction of incident visible light from the ordered air cavities (Fig. 2b). Comparing with the untreated macroporous PETPTA film displayed in Fig. S1d, an increase in wall thickness of the PHEMA/PETPTA voids is observed. As shown in Fig. 2c, the diffraction peak positions obtained from a macroporous PETPTA film templated from 255 nm silica particles, and a corresponding macroporous PHEMA/PETPTA film locate at 466 nm and 500 nm, respectively. The thickness of the coated PHEMA layer can then be estimated using $\lambda_{peak} = 2n_{eff} d \sin\theta$, where $n_{eff} = VF_{PETPTA} \times n_{PETPTA} + VF_{air} \times$

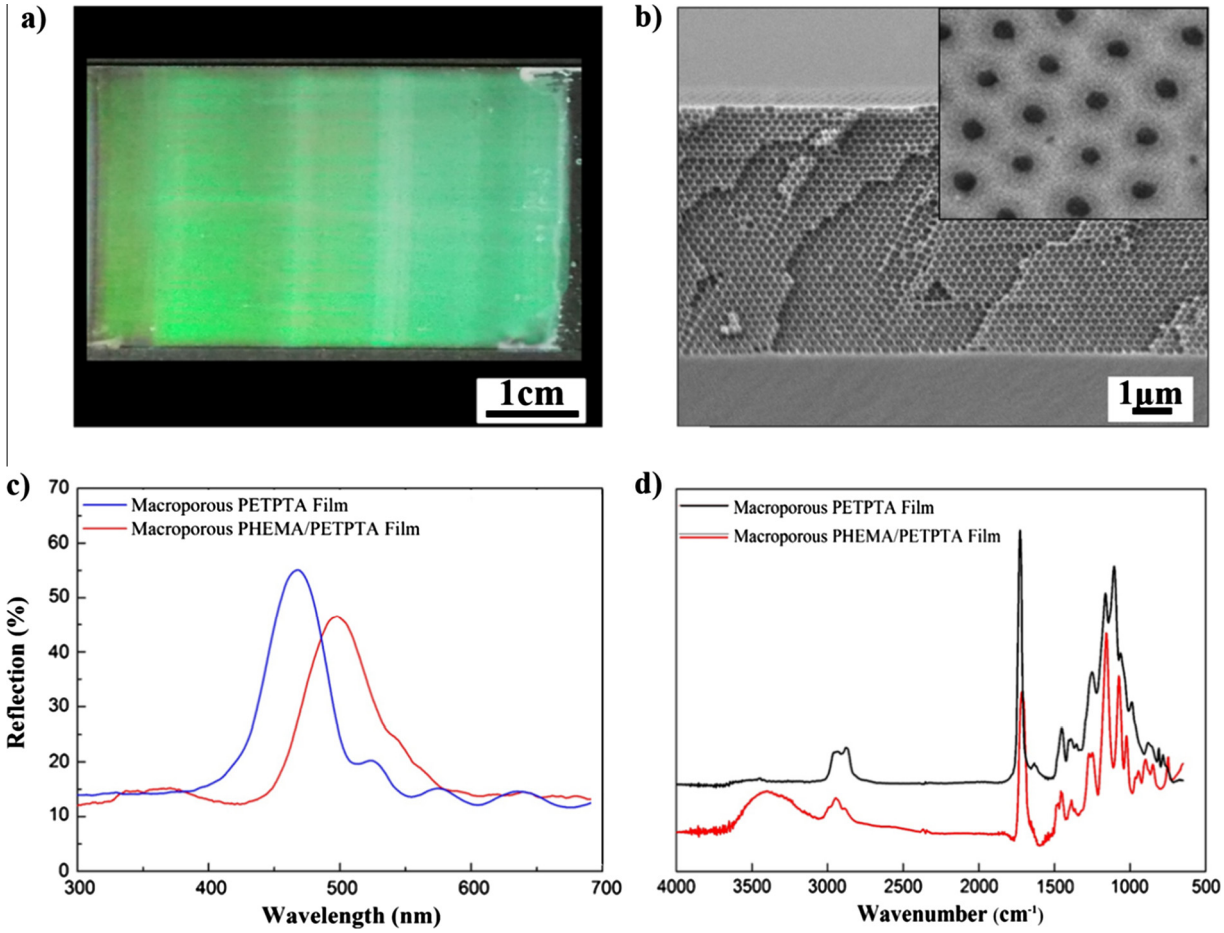

Fig. 2. (a) Photograph of a macroporous PHEMA/PETPTA film templated from 255 nm silica particles. (b) Cross-sectional SEM image of the same sample as in (a). Insert shows a magnified top-view SEM image. (c) Normal incidence specular reflection spectra of a macroporous PETPTA film templated from 255 nm silica particles, and a corresponding macroporous PHEMA/PETPTA film. (d) Fourier transform infrared spectra of the macroporous PETPTA film, and the macroporous PHEMA/PETPTA film.

$n_{air} + VF_{PHEMA} \times n_{PHEMA}$, and n_{PHEMA} equals to 1.45. The calculated result reveals that the volume fraction of PHEMA in the resulting macroporous film is around 14.8 vol.%, and a ~8.9 nm PHEMA layer can be coated on the walls of 255 nm voids. Besides, it is worthy to mention that excess amount of HEMA mixture retains in the coating procedure, leading to a thicker PHEMA layer coated on the film surface, and the formation of smaller void openings (Fig. 2b).

In order to identify that the PHEMA layer is coated on the films, Fourier transform infrared (FTIR) spectra of the macroporous PETPTA films with or without a PHEMA layer coating are analyzed using a PerkinElmer Spectrum 100 FTIR spectrometer (Fig. 2d). For untreated macroporous PETPTA films, the absorption peaks of carbonyl (C═O), bipyridine (C═C), and carboxylate (C—O) groups are observed at 1710, 1464, and 1256 cm^{-1}, respectively. In addition, it is noted in passing that bands occurring between 2600 and 3050 cm^{-1} are associated with the symmetric and antisymmetric C—H stretching vibrations of methylene (CH_2) and methyl (CH_3) groups [53]. In comparison with that, it is evident that a new wide adsorption peak centered at 3400 cm^{-1} appears for the PHEMA coating macroporous PETPTA films. The band is assigned to the OH stretching vibrations of PHEMA [54]. This further confirms the presence of PHEMA.

To evaluate the sensitivity and selectivity of vapor sensing for the as-prepared macroporous film, normal-incidence specular reflection spectra are collected from a macroporous PHEMA/PETPTA film templated from 255 nm silica particles exposed to vapors with different vapor pressures after 1 min. As noted from Fig. 3a, the diffraction efficiency of the macroporous PHEMA/PETPTA film decreases with the increase of ethanol vapor pressure, while the Bragg diffraction peak of that is red-shifted from 500 nm to 595 nm as the ethanol vapor pressure increases from 0 P_0 to 1 P_0. The PHEMA-based hydrogel swells when ethanol vapor condenses in the air cavities of the macroporous film, resulting in a lower dielectric contrast between the polymer and the enclosed materials and a higher effective refractive index of the diffractive medium. The resulting swelling therefore leads to the reduction of diffraction efficiency and the observed color changing from green to orange. Not only ethanol vapor sensing, the results in Fig. 3b present that the optical response of water vapor detection is similar with that of ethanol vapor detection. In addition to that, a 42 nm wavelength shift can be achieved when the macroporous PHEMA/PETPTA film is exposed to saturated water vapor at 25 ± 1 °C. It is noteworthy that the macroporous PHEMA/PETPTA film on exposure to ethanol vapors exhibits larger red-shift than that on exposure to water vapors (Fig. 3c). The Flory-Huggins theory can be employed to interpret the behavior of vapor sensing. Due to a more favorable free energy of mixing for the PHEMA with ethanol than with water, the PHEMA layer displays a higher degree of swelling as the macroporous film exposed to ethanol vapors, actuating a significant red-shift in diffraction [55].

Crosslinked PHEMA, being exposure to a good solvent, instead of dissolving completely, absorbs a portion of the solvent and subsequently swells. To investigate the swelling degree of PHEMA layer in the macroporous PHEMA/PETPTA film at different vapor partial pressures, the volume fractions of condensed liquid (VF_{liquid}) are calculated by applying the Bragg diffraction equation

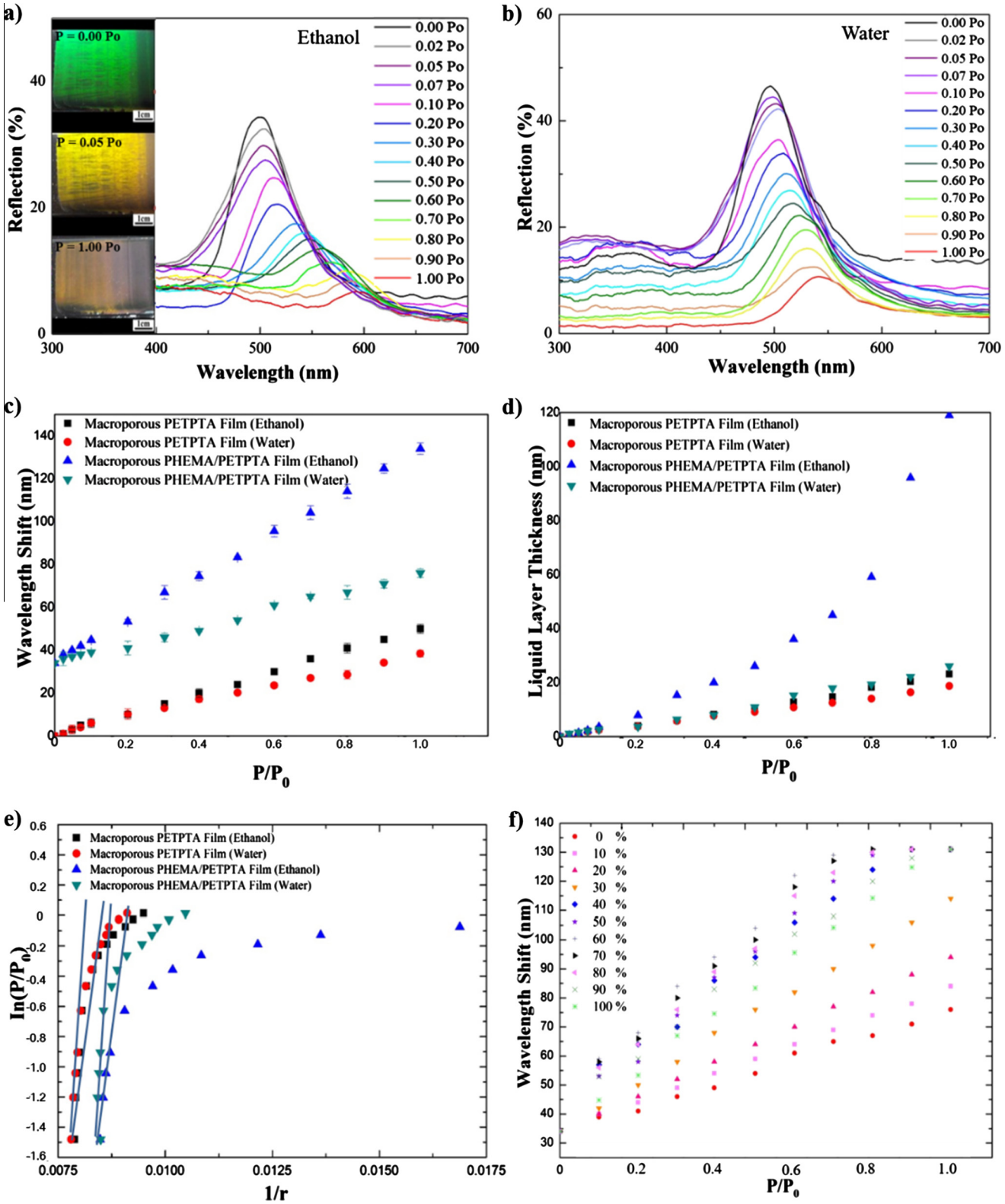

Fig. 3. (a) Photographic images and normal-incidence specular reflection spectra obtained from a macroporous PHEMA/PETPTA film templated from 255 nm silica particles exposed to ethanol vapors with different vapor pressures. (b) Normal-incidence specular reflection spectra obtained from the film exposed to water vapors with different vapor pressures. (c) Dependence of the shift of the Bragg diffraction peak on vapor partial pressure. (d) Calculated adsorbed condensed liquid layer thickness at different vapor partial pressures. (e) Dependence of $\ln(P/P_0)$ on the reciprocal of the radius of curvature of the condensed liquid films. (f) Dependence of the shift of the Bragg diffraction peak on different vapor pressure of ethanol/water mixtures.

in which $n_{eff} = VF_{PETPTA} \times n_{PETPTA} + VF_{PHEMA} \times n_{PHEMA} + VF_{air} \times n_{air} + VF_{liquid} \times n_{liquid}$, where VF_{PETPTA}, VF_{PHEMA}, and VF_{air} are 0.26, 0.15, and (0.59 – VF_{liquid}), respectively. By assuming the vapor condenses uniformly on the walls of the PHEMA/PETPTA voids and the PHEMA layer swells uniformly, the calculated VF_{liquid} can be used to estimate the extent of swelling in PHEMA, which can be expressed

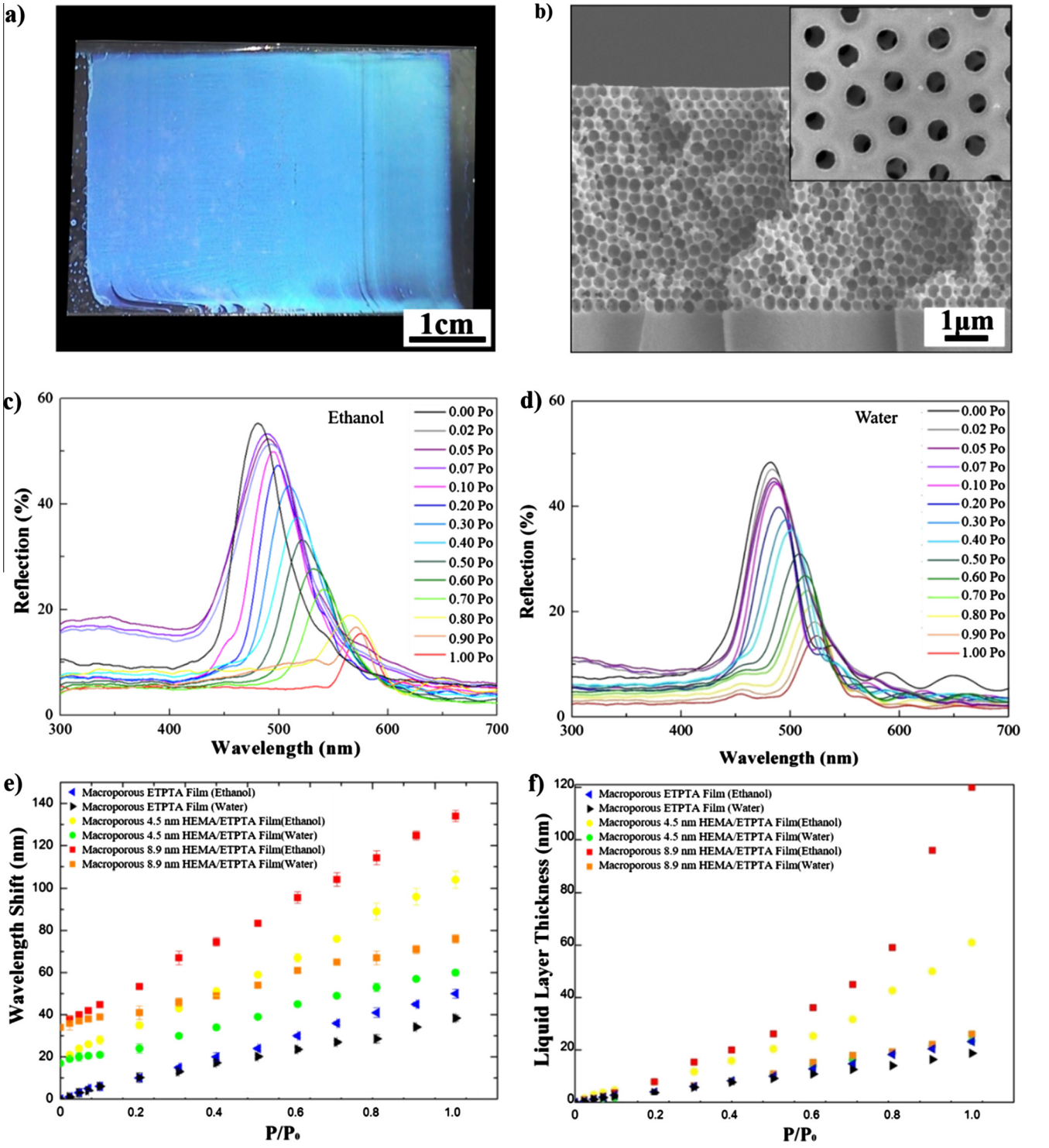

Fig. 4. (a) Photograph of a macroporous thin-PHEMA/PETPTA film templated from 255 nm silica particles. (b) Cross-sectional SEM image of the same sample as in (a). Insert shows a magnified top-view SEM image. (c) Normal-incidence specular reflection spectra obtained from the film exposed to ethanol vapors with different vapor pressures. (d) Normal-incidence specular reflection spectra obtained from the film exposed to water vapors with different vapor pressures. (e) Dependence of the shift of the Bragg diffraction peak on vapor partial pressure. (f) Calculated adsorbed condensed liquid layer thickness at different vapor partial pressures.

by condensed liquid layer thickness. Fig. 3d reveals that a thicker condensed liquid layer is associated with a higher vapor partial pressure. In addition to that, the calculated condensed ethanol layers are thicker than the condensed water layers at different vapor partial pressures. For instance, an around 26 nm condensed water layer can be formed when the macroporous PHEMA/PETPTA film is on exposure to a saturated water vapor, meanwhile a ~118 nm condensed ethanol layer can be formed in voids when the macroporous film is on exposure to a saturated ethanol vapor. In addition, the summation of PHEMA layer thickness and condensed ethanol liquid thickness equals to 126.9 nm, which is approximately equal to the pore radius (127.5 nm) of macroporous PETPTA photonic crystals. This indicates that the maximum thickness of PHEMA layer can be achieved by applying a 20 vol.% HEMA/ethanol mixture. To gain a better understanding, the Kelvin equation is used to describe the phenomenon of capillary condensation of a

condensable vapor and the resulting swelling in PHEMA. In macroporous photonic crystals, the radius of curvature of the swelling PHEMA/PETPTA void equals to the radius of the air cavity minus the calculated liquid layer thickness. As V_m, γ, R, and T are all constants, ln P/P_o is proportional to $1/r$. Fig. 3e displays that the experimental results of the vapor condensation in macroporous PETPTA films match reasonably well with the theoretical prediction. In contrast, this Kelvin equation only supports the experimental results of the ethanol vapor condensation in macroporous PHEMA/PETPTA films for low vapor partial pressures. The observed large deviation at higher ethanol vapor pressure is attributed to further swelling in PHEMA layer, leading to a greater amount of ethanol vapor condensation in the PHEMA-based film. Consequently, compared to the macroporous PETPTA film-based vapor sensing, the macroporous PHEMA/PETPTA film acts as a sensitive sensor for the presence of ethanol vapor. Additionally, the selectivity of vapor sensing is also further improved.

Fig. 3f summarizes the Bragg diffraction peak wavelength shift versus vapor partial pressure for different contents of ethanol/water vapor mixture. One can note that the diffraction peak wavelength increases not only with partial vapor pressure for each mixture, but also with the content of ethanol in the vaporous mixture. Interestingly, in the presence of ethanol content above 70%, the diffraction peak wavelength gradually decreases with increase in ethanol content in the vaporous mixture. The result is directly related to shrinking of the PHEMA layer, which can be understood by taking into account the hydrogen bonding of ester and amide C═O in the condensed mixed liquids [56–58]. The hydrogen bonding degree of ester and amide C═O in the aqueous mixture drastically decreases in ethanol concentrations above 70%, in which the shrinkage of the PHEMA starts.

5. PHEMA layer thickness effect on vapor-sensing

The PHEMA layer thickness effect on ethanol vapor sensing has been investigated in this study. The macroporous PETPTA film templated from 255 nm silica spheres is immersed in a 10 vol.% HEMA/ethanol mixture to fabricate macroporous thin-PHEMA/PETPTA photonic crystals. As shown in Fig. 4a, the as-prepared macroporous film displays a brilliant cyan color, which is caused by Bragg diffraction of incident visible light from the crystalline lattice of air cavities in the film (Fig. 4b). The reflection spectra in Fig. 4c disclose that the diffraction peak position collected from the resulting macroporous film on exposure to pure nitrogen locates at 483 nm, indicating the volume fraction of PHEMA in the macroporous film is around 7.5 vol.%, and an around 4.5 nm PHEMA layer can be coated on the walls of PETPTA voids. In addition, Fig. 4c and d presents that the results of ethanol vapor detection and water vapor detection are quite similar to those as shown in Fig. 3a and b. The shift of the diffraction peaks increases most linearly with vapor partial pressure (Fig. 4e). The thicker PHEMA layer results in a further increase in the amount of swelling in PHEMA, leading to a larger red-shift of the optical bands as the macroporous PHEMA/PETPTA film is exposed to ethanol vapors. It should be noted that the condensed ethanol layer in macroporous PHEMA/PETPTA film is thicker than that in macroporous thin-PHEMA/PETPTA film, while the condensed water layers in both macroporous films are with similar thickness (Fig. 4f). This demonstrates the sensitivity of ethanol vapor sensing is associated with coated PHEMA layer thickness.

6. Lattice spacing effect on vapor-sensing

Lattice spacing of macroporous photonic crystals is another parameter in determining the ethanol vapor sensing sensitivity. Therefore, we also conduct systematic investigations into the effect of lattice spacing on vapor sensing. The macroporous PETPTA films with smaller lattice spacing are templated from 173 nm silica particles (Fig. 5a), following by immersing in a 20 vol.% HEMA/ethanol mixture to coat with a uniform layer of PHEMA in the PETPTA voids (Fig. 5b). As demonstrated previously, the macroporous PETPTA photonic crystal-based vapor sensing can be applied to ethanol vapor and water vapor. Fig. 5c and d reveals that the optical response of ethanol vapor sensing is similar to that of water vapor sensing. In contrast, a maximum wavelength shift of 59 nm can be achieved when the macroporous PHEMA/PETPTA film is exposed to a saturated ethanol vapor, whereas a 22 nm wavelength shift is achieved as the water vapor partial pressure increases from 0 P_0 to 1 P_0 (Fig. 5e and f). The results indicate that the macroporous PHEMA/PETPTA film on exposure to ethanol vapors displays larger red-shift than that on exposure to water vapors. Although macroporous PHEMA/PETPTA films with decreasing lattice spacing exhibit smaller red-shift on vapor sensing, it is observed that the diffraction peak shifts from 339 nm to 398 nm on ethanol vapor sensing, which can easily monitor the ethanol vapor pressure based on the film color dramatically changing from transparent to violet (inserts in Fig. 5e).

Moreover, the vapor sensing for macroporous photonic crystals with larger lattice spacing is investigated. The macroporous PETPTA films consisting crystalline lattice of 325 nm air cavities are immersed in a 20 vol.% HEMA/ethanol mixture, following by a photo-polymerization process. A uniform PHEMA layer coated on the macroporous PETPTA films is clearly seen from Fig. 6a and b. Compared to macroporous PETPTA photonic crystal vapor sensing as shown in Fig. 6c and d, the reflection spectra in Fig. 6e and f confirm that the macroporous PHEMA/PETPTA polymer films display higher sensitivity on vapor sensing. It is pertinent to note that the diffraction peak of macroporous PHEMA/PETPTA film templated from 325 nm silica particles shifts from 637 nm to 757 nm as the ethanol vapor partial pressure increases from 0 P_0 to 1 P_0. The resulting 120 nm red-shift in wavelength leads to the film color changing from red to transparent (inserts in Fig. 6e). Therefore, it is effective to develop naked-eye detector for ethanol vapor pressure changes by adjusting the lattice spacing of macroporous photonic crystals.

7. Reproducibility of vapor sensing

It is significant to note that the shift of the diffraction peaks increases in a nearly linear relation with vapor partial pressure. The linear response is critical to determine the vapor contents. Importantly, the optical properties of the macroporous photonic crystals can be fully recovered as the condensed liquid is evaporated and can thus be reused for vapor sensing. The reproducibility of macroporous PHEMA/PETPTA films template from 255 nm silica spheres for ethanol vapor sensing is studied in this research. The Bragg diffraction peak of the macroporous film is red-shifted from 500 nm to 595 nm after exposure to saturated ethanol vapor. Then the film is exposed to pure nitrogen and saturated ethanol vapor alternately for several cycles to evaluate its durability. In Fig. 7, the black blocks and red circles represent the diffraction peak position of the film after exposure to pure nitrogen and saturated ethanol vapor for 1 min, respectively. The conversion of the diffraction peak position upon exposure to pure nitrogen and saturated ethanol vapor is reversible and repeatable after 100 cycles. The use of macrporous PETPTA as a scaffold presumably limits inhomogeneous deformation of PHEMA hydrogel during the cycles, resulting in a great reversibility and reproducibility for ethanol vapor sensing.

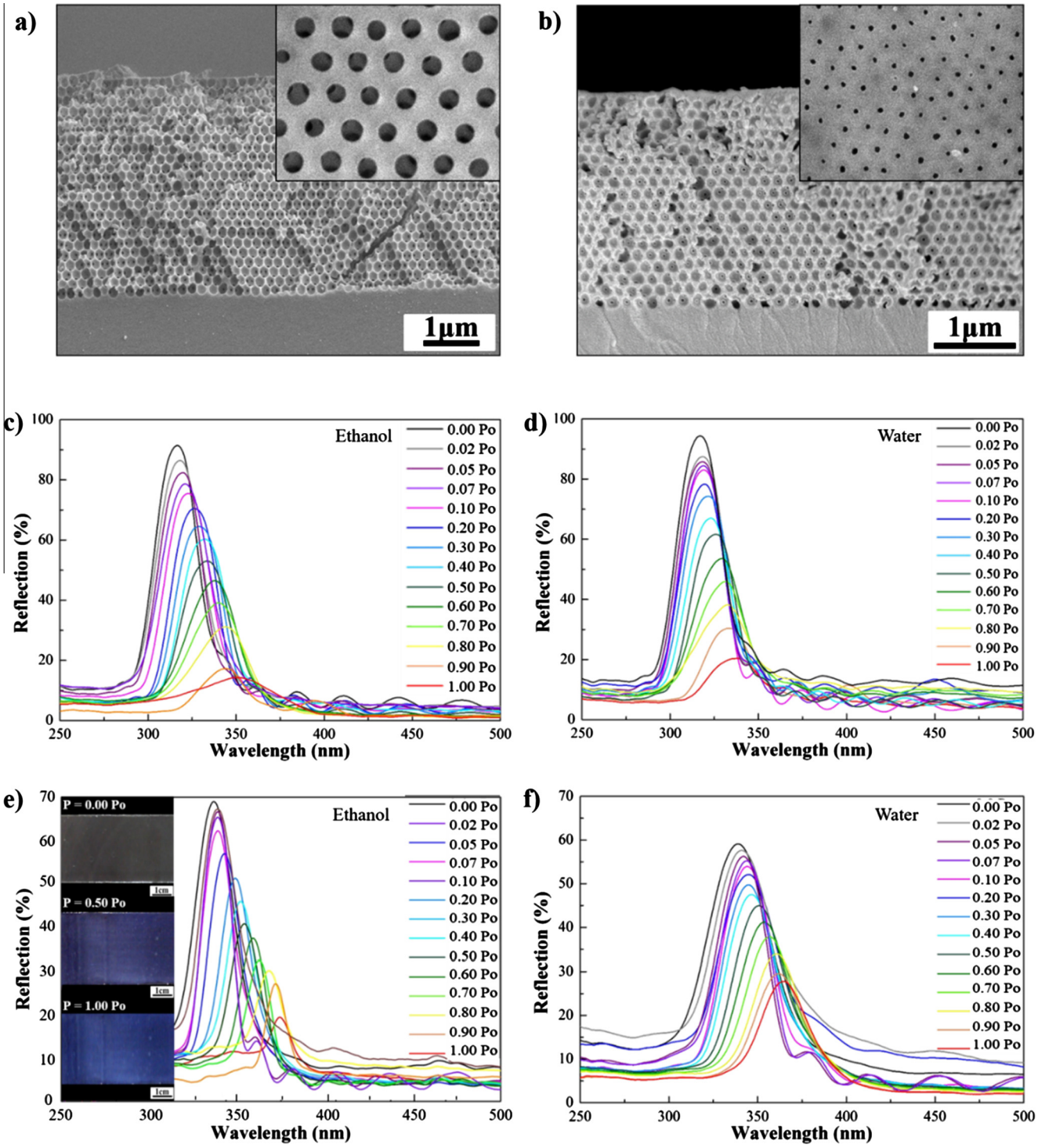

Fig. 5. (a) Cross-sectional SEM image of a macroporous PETPTA film consisting of 173 nm air cavities. Insert shows a magnified top-view SEM image. (b) Cross-sectional SEM image of a macroporous PHEMA/PETPTA film templated from 173 nm silica particles. Insert shows a magnified top-view SEM image. (c) Normal-incidence specular reflection spectra obtained from a macroporous PETPTA film consisting of 173 nm air cavities exposed to ethanol vapors with different vapor pressures. (d) Normal-incidence specular reflection spectra obtained from the macroporous PETPTA film exposed to water vapors with different vapor pressures. (e) Photographic images and normal-incidence specular reflection spectra obtained from a macroporous PHEMA/PETPTA film templated from 173 nm silica particles exposed to ethanol vapors with different vapor pressures. (f) Normal-incidence specular reflection spectra obtained from the macroporous PHEMA/PETPTA film exposed to water vapors with different vapor pressures.

8. Conclusions

In summary, 3D macroporous hydrogel photonic crystals is fabricated by the combination of doctor blade coating technique and templating method. The photonic crystals not only provide a highly visible readout, but also display fast response rate and large stop band shift for ethanol vapor response. The highly ordered macroporous structure can even quantitatively analyze vapor-phase ethanol, and has shown promising sensitivity. Moreover, the vapor sensing performances can be further improved by controlling the coated hydrogel layer thickness and the lattice spacing of macroporous photonic crystals. Owing to the intrinsic characteristics of PHEMA, the macroporous PHEMA/PETPTA photonic crystals are most sensitive to 60%–

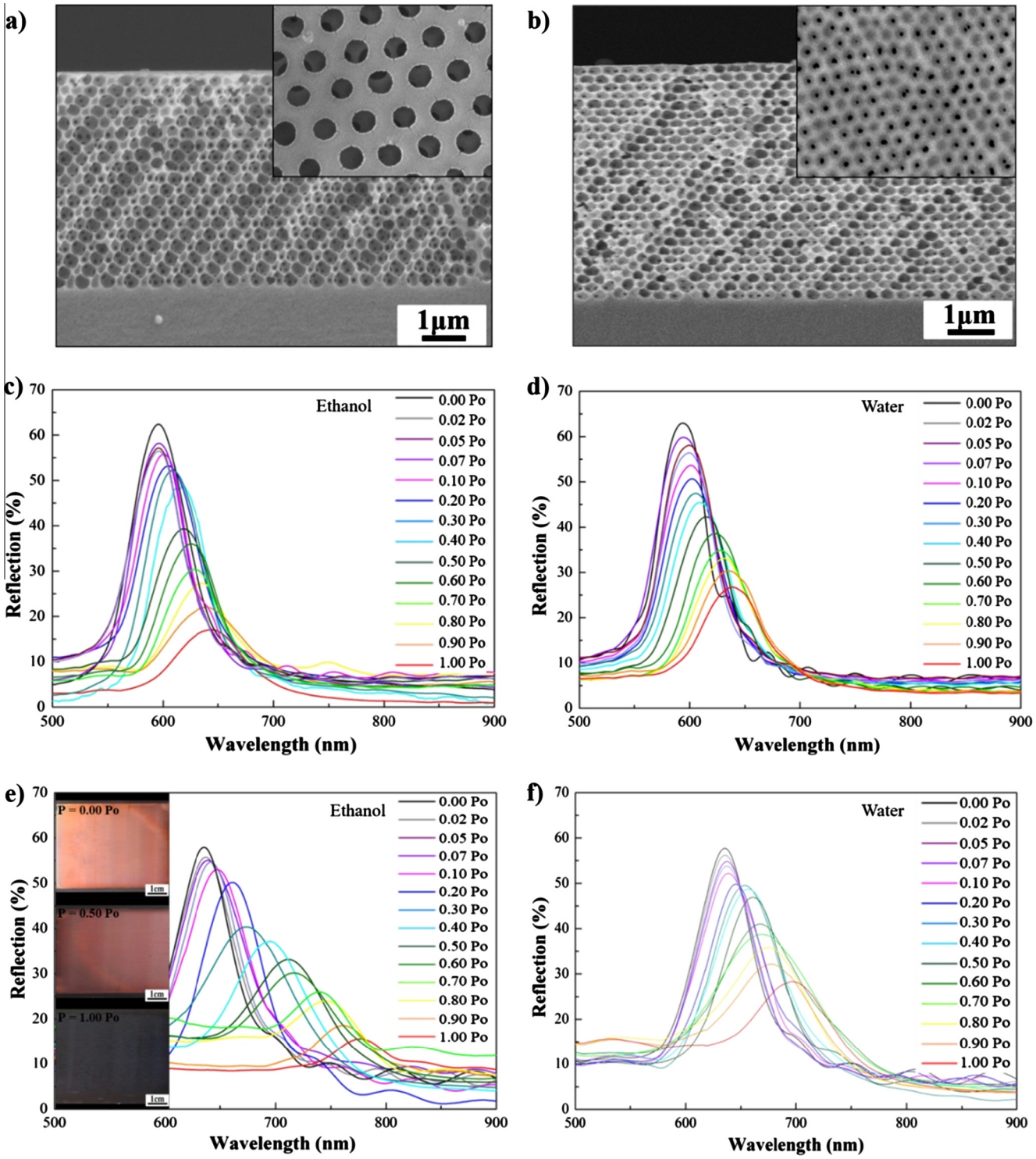

Fig. 6. (a) Cross-sectional SEM image of a macroporous PETPTA film consisting of 325 nm air cavities. Insert shows a magnified top-view SEM image. (b) Cross-sectional SEM image of a macroporous PHEMA/PETPTA film templated from 325 nm silica particles. Insert shows a magnified top-view SEM image. (c) Normal-incidence specular reflection spectra obtained from a macroporous PETPTA film consisting of 325 nm air cavities exposed to ethanol vapors with different vapor pressures. (d) Normal-incidence specular reflection spectra obtained from the macroporous PETPTA film exposed to water vapors with different vapor pressures. (e) Photographic images and normal-incidence specular reflection spectra obtained from a macroporous PHEMA/PETPTA film templated from 325 nm silica particles exposed to ethanol vapors with different vapor pressures. (f) Normal-incidence specular reflection spectra obtained from the macroporous PHEMA/PETPTA film exposed to water vapors with different vapor pressures.

70% ethanol/water mixtures. Although the use of PHEMA may restrict the practical application for ethanol vapor sensing, the use of macrporous templated scaffold leads to a great reversibility and reproducibility for vapor sensing. We believe that our method can provide a simple and scalable route for preparing portable macroporous hydrogel photonic crystals with various functional groups to expand the responsive ability, which may find great potential applications in the field of pH monitoring, temperature detection, optical switching, chemical/biological sensing, etc.

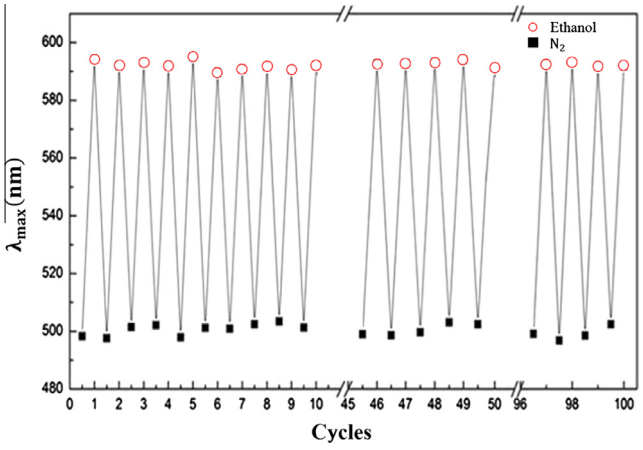

Fig. 7. Reproducible ethanol vapor sensing of a macroporous PHEMA/PETPTA film templated from 255 nm silica particles.

Acknowledgments

Acknowledgment is made to Ministry of Science and Technology (Grant MOST 104-2221-E-005-086 and MOST 103-2622-E-005-017-CC3) for support of this research.

Appendix A. Supplementary material

Supplementary data associated with this article can be found, in the online version, at http://dx.doi.org/10.1016/j.jcis.2016.10.061.

References

[1] W.K. Boyes, L.L. Degn, S.A. Martin, D.F. Lyke, C.W. Hamm, D.W. Herr, Neurotoxicol. Teratol. 43 (2014) 1–10.
[2] C. Bartual, A. Akou, C. Thibault, C. Vieu, L. Salmon, A.J. Bousseksou, Mater. Chem. C 3 (2015) 1277–1285.
[3] X. Yu, N. Zhou, S. Han, H. Han, D. Buchholzn, J.J. Yu, Mater. Chem. C 1 (2013) 6532–6535.
[4] G.L. Shang, G.T. Fei, Y. Zhang, P. Yan, S.H. Xu, L.D.J. Zhang, Mater. Chem. C 1 (2013) 5285–5291.
[5] R.K. Niven, Renew. Sustain Energy Rev. 9 (2005) 535–555.
[6] M.R. Cook, F.J. Bergman, H.D. Cohen, M.M. Gerkovich, C. Graham, R.K. Harris, L. G. Siemann, Res. Rep. Health Eff. Inst. 42 (1991) 1–45.
[7] C.H. Kwak, H.S. Woo, F. Abdel-Hady, A.A. Wazzan, J.H. Lee, Sens. Actuator B-Chem. 223 (2016) 527–534.
[8] M. Wang, L. Zhu, C. Zhang, G. Gai, X. Ji, B. Li, Y. Yao, Sens. Actuator B-Chem. 224 (2016) 478–484.
[9] J. Hodgkinson, R.P. Tatam, Meas. Sci. Technol. 24 (2013) 012004.
[10] S. Mao, G. Lu, J.J. Chen, Mater. Chem. A 2 (2014) 5573–5579.
[11] M. Konstantaki, A. Klini, D. Anglos, S. Pissadakis, Opt. Express 20 (2012) 8472–8484.
[12] M.H. Darvishnejada, A.A. Firooz, J. Beheshtian, A.A. Khodadadi, RSC Adv. 6 (2016) 7838–7845.
[13] O.S. Wolfbeis, Anal. Chem. 80 (2008) 4269–4283.
[14] X. Liu, S.T. Cheng, H. Liu, S. Hu, D.Q. Zhang, H.S. Ning, Sensors 12 (2012) 9635–9665.
[15] J.J. Shi, Y.F. Zhu, X.R. Zhang, W.R.G. Baetens, A.M. Gaecia-Campana, TRAC, Trends Anal. Chem. 23 (2004) 351–360.
[16] J.D. Joannopolos, P.R. Villeneuve, S.H. Fan, Nature 386 (1997) 143–149.
[17] L. Bai, Z. Xie, L. Cao, Y. Zhao, H. Xu, C. Zhu, Z. Mu, Q. Zong, Z. Gu, Nanoscale 6 (2014) 5680–5685.
[18] H. Xu, P. Wu, C. Zhu, A. Elbaz, Z.Z.J. Gu, Mater. Chem. C 1 (2013) 6087–6098.
[19] R.A. Potyrailo, H. Ghiradella, A. Vertiatchikh, K. Dovidenko, J.R. Cournoter, E. Olson, Nat. Photon. 1 (2007) 123–128.
[20] H. Yang, P. Jiang, B. Jiang, J. Colloid Interface Sci. 370 (2012) 11–18.
[21] Y. Zhao, Y.N. Zhang, Q. Wang, Sens. Actuator B 160 (2011) 1288–1297.
[22] Y.J. Zhao, Z.T. Xie, H.C. Gu, C. Zhu, Z.Z. Gu, Chem. Soc. Rev. 41 (2012) 3297–3317.
[23] J.P. Ge, Y.D. Yin, Angew. Chem. Int. Ed. 50 (2011) 1492–1522.
[24] E. Redel, P. Mirtchev, C. Huai, S. Petrov, G.A. Ozin, ACS Nano 5 (2011) 2861–2869.
[25] Y. Yamada, M. Ishii, T. Nakamura, K. Yuan, Langmuir 26 (2010) 10044–10049.
[26] L.D. Stefano, L. Rotirote, E.D. Tommasi, I. Rea, I. Rendina, M. Canciello, G. Maglio, R. Palumbo, J. Appl. Phys. 106 (2009). p. 023109-023109-5.
[27] T. Nakamura, Y. Yamada, H. Yamada, K. Yano, J. Mater. Chem. 19 (2009) 6699–6705.
[28] L. Bai, Z. Xie, K. Cao, Y. Zhao, H. Xu, C. Zhu, Z. Mu, Q. Zhong, Z. Gu, Nanoscale 6 (2014) 5680–5685.
[29] E. Istrate, E.H. Sargent, Rev. Mod. Phys. 78 (2006) 455–481.
[30] J.H. Kang, J.H. Moon, S.K. Lee, S.G. Park, S.G. Jang, S. Yang, S.M. Yang, Adv. Mater. 20 (2008) 3061–3065.
[31] K. Matsubara, M. Watanabe, Y. Tokeoka, Langmuir 22 (2006) 4403–4407.
[32] R. Pernice, G. Adamo, S. Stivala, A. Parisi, A.C. Busacca, D. Spigolon, M.A. Sabatino, L. D'Acquisto, C. Dispenza, Opt. Mater. Express 3 (2013) 1820–1833.
[33] L. Nucara, F. Greco, V.J. Mattoli, Mater. Chem. C 3 (2015) 8449–8467.
[34] X. Ye, Y. Li, J. Dong, J. Xiao, Y. Ma, L.J. Qi, Mater. Chem. C 1 (2013) 6112–6119.
[35] L. Lonov, Mater. Today 17 (2014) 494–503.
[36] P. Lodahl, S. Mahmoodian, S. Stobbe, Rev. Mod. Phys. 87 (2015) 347–400.
[37] A. Biswas, I.S. Bayer, A.S. Biris, T. Wang, E. Dervishi, F. Faupel, Adv. Colloid Interface Sci. 170 (2012) 2–27.
[38] J. Lee, J. Seo, D. Kim, S. Shin, S. Lee, C. Mahata, H. Lee, B. Min, T. Lee, ACS Appl. Mater. Interfaces 6 (2014) 9053–9060.
[39] S. Wong, V. Kitaev, G.A. Ozin, J. Am. Chem. Soc. 125 (2003) 15589–15598.
[40] A. Dong, J. Chen, P.M. Vora, J.M. Kikkawa, C.B. Murry, Nature 466 (2010) 474–477.
[41] N.D. Denkov, O.D. Velev, P.A. Kralchevsky, I.B. Ivanov, H. Yoshimura, K. Nagayama, Nature 361 (1993) 26.
[42] T.H. Lin, W.H. Huang, I.K. Jun, P. Jiang, Chem. Mater. 21 (2009) 2039–2044.
[43] H.L. Li, J.X. Wang, L.M. Yang, Y.L. Song, Adv. Funct. Mater. 18 (2008) 3258–3264.
[44] E.T. Tian, J.X. Wang, Y.M. Zheng, Y.L. Song, L. Jiang, D.B.J. Zhu, Chem. Mater. 18 (2008) 1116–1122.
[45] C.H. Sun, P. Jiang, Nat. Photon. 2 (2008) 9–11.
[46] C.-Y. Cai, K.-Y. Lin, H. Yang, Appl. Phys. Lett. 105 (2014) 201913-1–201913-5.
[47] W. Stöber, A. Fink, E.J. Bohn, J. Colloid Interface Sci. 26 (1968) 62–69.
[48] H. Yang, P. Jiang, Langmuir 26 (2010) 13173–13182.
[49] P. Jiang, J.F. Bertone, K.S. Hwang, V.L. Colvin, Chem. Mater. 11 (1999) 2132–2140.
[50] R. Pernice, G. Adamo, S. Stivala, A. Oarisi, A.C. Busaccam, D. Spigolon, M.A. Sabatino, L. D'Acquisto, C. Dispenza, Opt. Mater. Express 3 (2013) 1820–1833.
[51] D. Lide, H. Frederikse, Handbook of Chemistry and Physics, CRC Press Inc., Boca Raton, FL, 1995.
[52] L.R. Fisher, R.A. Gamble, J. Middlehurst, Nature 290 (1981) 575–576.
[53] H. Yang, P. Jiang, Appl. Phys. Lett. 98 (2011) 011104-1–011104-3.
[54] Y. Qi, X. Meng, J. Yang, Z. Zeng, Y. Chen, J. Appl. Polym. Sci. 96 (2005) 846–853.
[55] T.S. Perova, J.K. Vij, H. Xu, Colloid Polym. Sci. 275 (1997) 323–332.
[56] X. Xu, A.V. Goponenko, S.A. Asher, J. Am. Chem. Soc. 130 (2008) 3113–3119.
[57] A. Hiroki, Y. Maekawa, M. Yoshida, K. Kubota, R. Katakai, Polymer 42 (2001) 1863–1867.
[58] A.G. Mayes, J. Blyth, M. Kyrolainen-Reay, R.B. Millington, C.R. Lowe, Anal. Chem. 71 (1999) 3390–3396.